

# Parameters Influencing Electrodeposition of Nanocrystalline $\text{Fe}_x\text{--Co}_{100-x}$ Alloys on Stainless Steel

Santosh Kumar Nathsharma<sup>a</sup>, Sasmita Mishra<sup>a</sup>,  
Krushna Gopal Mishra<sup>a, \*</sup>, and Raja Kishore Paramguru<sup>b</sup>

<sup>a</sup> School of Applied Sciences, Kalinga Institute of Industrial Technology Deemed to be University,  
Bhubaneswar, Odisha, 751024 India

<sup>b</sup> School of Mechanical Engineering, Kalinga Institute of Industrial Technology Deemed to be University,  
Bhubaneswar, Odisha, 751024 India

\*e-mail: kgmishrafch@kiit.ac.in

Received October 5, 2020; revised January 8, 2021; accepted January 12, 2021

**Abstract**—Nanocrystalline Fe–Co alloys were electrodeposited on stainless steel from sulfate baths using citrate as a complexing agent. The citrate helped in reducing the standard reduction potentials of both Cocitrate and Fecitrate to closer values for the co-deposition of the alloys. The calculated kinetic parameter data obtained from the cathodic polarisations were used to understand the mechanism of the electron transfer in the deposition of alloys. A significant influence of the parametric conditions such as the composition of the electrolytic solution, pH, current density, and temperature on the cathodic current efficiency, and the composition of the deposit of Fe–Co alloys was studied. The nucleation potential of the alloys (–0.88 V) was closer to the nucleation potential of Co (–0.84 V) than to that of Fe (–0.94 V). There was a shift of the nucleation potential to a more cathodic value (–1.17 V) by lowering  $[\text{Co}^{2+}]$  whereas only a small variation was observed in lowering  $[\text{Fe}^{2+}]$ . The current efficiency was found to increase from 59.4 to 81.1% by increasing  $[\text{Co}^{2+}]$  from 0.025 to 0.200 M at fixed  $[\text{Fe}^{2+}]$  of 0.100 M. The cobalt percentage in the alloys was found to increase from 48.6 to 54.3% by changing pH from 2 to 4. Both cobalt and iron contents in the alloys were found to increase via increasing the concentration of individual ions in the plating bath. The crystallographic structure of the electrodeposited alloys reveals the formation of a single solid solution phase with the body-centered cubic structure. The spherical deposit of nanosized Fe–Co alloys was observed via scanning electron microscopy. There was an attempt to correlate the iron content, the average grain size, and crystallographic orientation with saturation magnetization and lower coercivity.

**Keywords:** electroplating, Fe–Co alloys, current efficiency, electrokinetic parameter, current density

**DOI:** 10.3103/S1068375522010069

## INTRODUCTION

Magnetic nanomaterials are in the focus of researchers' interests owing to their unique properties such as super paramagnetism, high surface area, and dispersity in solutions [1]. The potential uses of such materials broadly range from biomedical imaging, medical diagnostics and magnetic memory devices to catalysis, environment remediation, optical filters, and defect sensors. The magnetic nonmaterials being studied are iron oxides and metals such as iron, cobalt, nickel, copper, zinc, manganese, barium and strontium. Recently, nanoparticles of metals like Fe, Cu, Ni, Co and some of their alloys have been successfully produced. Moderately high saturation magnetization is usually achieved in the NiFe-based nanomaterials. Recently, Fe–Co based nanomaterials have received increasing attention due to their immense applications.

Fe–Co alloys occupy an important position because of their unique magnetic properties and usage areas such as magnetic shielding, micro and nano-electromechanical systems [2, 3], electronic sensors [4], high Curie temperatures [5], magnetic recording head cores in data storage devices [6–10], they also have high permeability, low losses, and relative strength [11, 12]. The unique magnetic properties may be owing to their higher achievable saturation magnetization ( $B_s$ ) and lower coercivity ( $H_c$ ) [13–18]. In magnetic data storage applications, ferromagnetic nanoparticles possessing high  $B_s$  and  $H_c$  are studied for usage in high-density magnetic media such as magnetic recording write heads [19–21]. Therefore, Fe–Co alloy production was chosen for this study and also because the system developed can easily be extended for correlating with the magnetic property.

Various methods for producing Fe–Co alloys have been reported over the years. The routes include both

pyro- and hydro-based processes such as combustion synthesis, carbon arc, laser pyrolysis, low temperature hydrogen plasma from the oxides, chemical vapor deposition, thermal decomposition, co-precipitation, micro-emulsion, electroplating, and electroless deposition. All these methods generally involve multiple unit processes, such as melting a required composition of alloy in a heating furnace, followed by casting, hot rolling, quenching, cold rolling, annealing, and so on. Among these techniques, electrodeposition stands as one of the most attractive processing routes [22–24] owing to its ease of production, low cost, and ability to precisely control the nanomaterials of the desired size and deposit thickness, which, in turn, monitors  $B_s$  and  $H_c$ . This is the main motivation for the present study.

Industrially speaking, only a few alloys systems have been commercialised because an ample control of these complex processes is usually required to obtain a correct understanding of their kinetics and mechanisms. Thus, in order to improve the Fe–Co alloys magnetic properties, the origin of their microstructure and the growth kinetics need to be understood. It is reported elsewhere that the cobalt content is increased from 40 to 85% on increasing the molar ratio  $[\text{Co}^{2+}]/[\text{Fe}^{2+}]$  from 0.5/0.5 to 0.90/0.1, and the same cobalt content is decreased from 77 to 63% when pH is raised from 2.1 to 4.3 [25]. The compositional and structural analysis of electrodeposited Fe–Co films at different temperatures was presented in [26]. There the authors have found that at a temperature below 40°C, preferentially iron is deposited, but with an increase in temperature, the cobalt deposition is increased. The electroplated films prepared at 30 and 40°C have only the body-centered cubic (bcc) phase, but at room temperature mixed (bcc + face-centered cubic (fcc)) lattices are found [26]. The authors in [25] demonstrated that the crystal texture of the deposited alloys strongly depends on the metal ion concentration, the amount of a buffer and of a complexing agent.

In addition to all these inputs, the mechanism and the influence of other parametric conditions on the electrokinetic behavior are also very important in the deposition of alloys [27]. There is hardly any study available on the kinetic parameters of the anomalous deposition of Fe–Co alloys on the stainless steel (SS) electrode. Though there are plenty of publications on the deposition of individual metal: Co, Cu, Fe, Ni, Mn, etc. using SS, Cu, Ti, or glass carbon as cathode electrodes, and on the cathodic current efficiency (CCE) with them, there are just a few publications on the alloy deposition on the SS electrode as well as on the CCE in this case. The fundamental and thin film study of the alloys has been reported by many researchers using glassy carbon, Pt or the mentioned above electrodes. The review [28] reports the CCE of the alloys as 64–90% in a pyrophosphate bath. The current efficiency from Co and Fe% determined via atomic absorption spectrometry was given in [29].

Others reported in [30] the CCE of 69.45–75.12% as a function of the current density by using SS as cathode material. The SS cathodes are usually employed in the commercial production of metals and alloys. So, the results of such fundamental studies using the SS electrode can be of immense help to improve the industrial production with good quality and quantity of the alloys.

Thus, the purpose of the present research was to study the influence of the parametric conditions and the kinetic parameters in the Fe–Co alloys deposition process on the SS electrode. Besides, the key factor influencing the formation of Fe–Co alloys and the effect on the deposit composition, its surface morphology and crystallographic structures are also discussed in this work. In addition, a comparison was made to correlate the effect of the average particle size of the alloys found in the present study on the magnetic property reported by others.

## EXPERIMENTAL

The Fe–Co alloys were electroplated on mechanically polished and cleaned SS 304 electrode from the baths with the compositions shown in Table 1. All chemicals were of the laboratory analytical grade. All solutions were freshly prepared with distilled water. The pH of the plating solution was adjusted using NaOH (Merck) and was measured using a Systronics 335 digital pH meter. A Pb–Sb (6–7% Sb) sheet was used as the anode. The anode material had dimensions of  $4 \times 6$  cm exposed for plating. The electrodeposition (see Fig. 1 with the electrodeposition set up) was carried out from stationary solutions. An Aplab, India make, external DC source, was used as the current source, and a Picotest multimeter was used to record the cathode and anode potentials vs. saturated calomel electrode (SCE) during all deposition processes. The experiments were conducted at the required temperatures with the help of a water bath from Thermo Scientific, UK. The duration of electrodeposition was 1h in all experiments. Then the SS cathode was withdrawn, washed with distilled water followed by acetone (Merck) and finally dried and weighed. The cyclic voltammograms (CVs) of deposition were conducted in a three-electrode cell provided with an SS plate of area  $1 \text{ cm}^2$  used as a working electrode. A platinum plate of  $1 \text{ cm}^2$  area was used as a counter electrode, and SCE as a reference electrode. The potential of the working electrode was measured by a Princeton Applied Research potentiostat (PARSTAT 4000, USA). The crystallographic study of the electroplated Fe–Co film was measured via X-ray diffraction (XRD) (device model Empyrean, Panalytical). The surface structure and morphology were characterized via scanning electron microscopy (SEM) (device model EVO 18, Carl Zeiss). The elemental analysis of the deposited film was analyzed by

**Table 1.** Composition and operating conditions of electroplating bath for Fe, Co, and Fe–Co alloys

Compound	Concentration
FeSO <sub>4</sub> ·7H <sub>2</sub> O (Merck, 99%)	0.025–0.2 M
CoSO <sub>4</sub> ·7H <sub>2</sub> O (Merck, 99%)	0.025–0.2 M
Sodium citrate (SRL, 99%)	0.05 M
MgSO <sub>4</sub> (Merck, 98%)	0.05 M
H <sub>3</sub> BO <sub>3</sub> (Merck, 99.5%)	0.04 M
pH	2–4
Current density	30–70 mA cm <sup>-2</sup>
Temperature	R.T–70°C
Anode	Pb–Sb
Cathode	SS304

energy dispersive spectroscopy (EDS) (analyzer from Ametek, EDAX, USA).

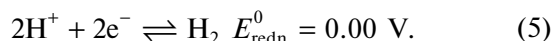
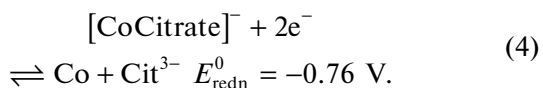
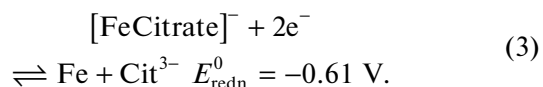
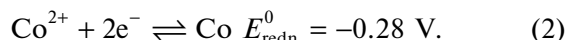
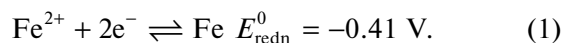
## RESULTS AND DISCUSSION

### Polarisation Curves

The cathodic polarisation study of the Fe–Co alloy system was conducted in the electrolyte containing: 0.025–0.200 M FeSO<sub>4</sub>·7H<sub>2</sub>O, 0.025–0.200 M CoSO<sub>4</sub>·7H<sub>2</sub>O, 0.050 M sodium citrate, 0.050 M MgSO<sub>4</sub>, and 0.040 M H<sub>3</sub>BO<sub>3</sub>. The purpose of using sodium citrate as a complexing agent was not only to reduce the large difference of the standard reduction potential ( $E_{\text{redn}}^0$ ) values in the couples Fe<sup>2+</sup>/Fe (–0.41 V) and Co<sup>2+</sup>/Co (–0.28 V) but also its high stability to inhibit the decomposition of bath solutions and to control the reaction with the substrate surface.

MgSO<sub>4</sub> was used as a supporting electrolyte and H<sub>3</sub>BO<sub>3</sub> as a buffering reagent to maintain the bath pH at different conditions. The citrate complex of Fe<sup>2+</sup> and Co<sup>2+</sup> ions forms a soluble electrolytic solution and

reduces to form the alloys according to the following reaction scheme:



The cathodic and anodic polarisation segments of the CVs in Fig. 2 are comprised of the cathodic reduction for the metal and alloys deposition (nucleation with growth), the hydrogen evolution, the crossover regime (crossover potential), and the anodic dissolution. The corresponding peaks and processes are in Fig. 2: curves *a*, *b*, and *c* for Co, Fe, and Fe–Co alloy, respectively.

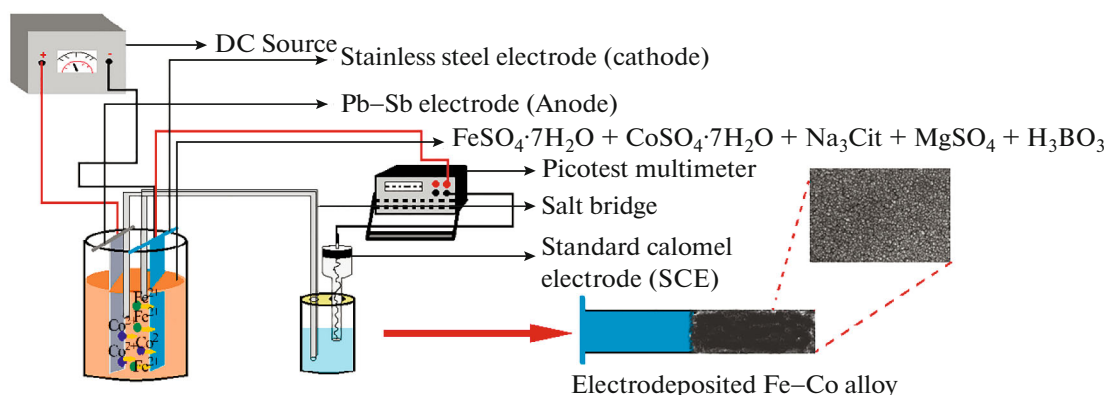


**Fig. 1.** Schematic set up used for electrodeposition of Fe–Co alloys.

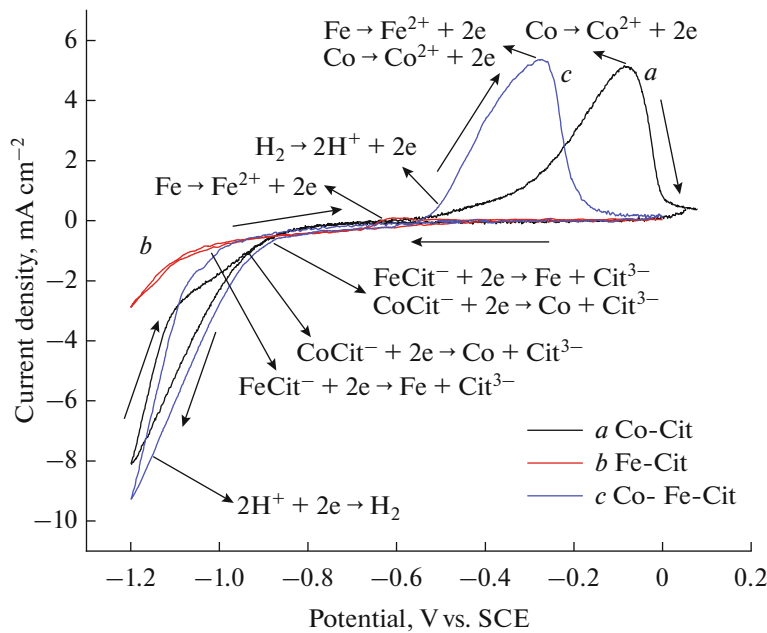


**Fig. 2.** CVs of Fe, Co, and Fe–Co alloy electrodeposition at a scan rate of  $10 \text{ mV s}^{-1}$ . Bath condition: 0.05 M sodium citrate, 0.05 M  $\text{MgSO}_4$ , 0.40 M  $\text{H}_3\text{BO}_3$ , pH 4, and temperature  $25^\circ\text{C}$  with: (a) 0.1 M  $[\text{Co}^{2+}]$ , (b) 0.1 M  $[\text{Fe}^{2+}]$ , (c) 0.1 M  $[\text{Co}^{2+}]$ , and 0.1 M  $[\text{Fe}^{2+}]$ .

The cathodic polarisation in Fig. 3, curve *a*, of the CV at 0.1 M  $[\text{Co}^{2+}]$  shows an increase in the current density that begins at an applied voltage of  $-0.83 \text{ V}$  due to the deposition of Co. The cathodic polarisation

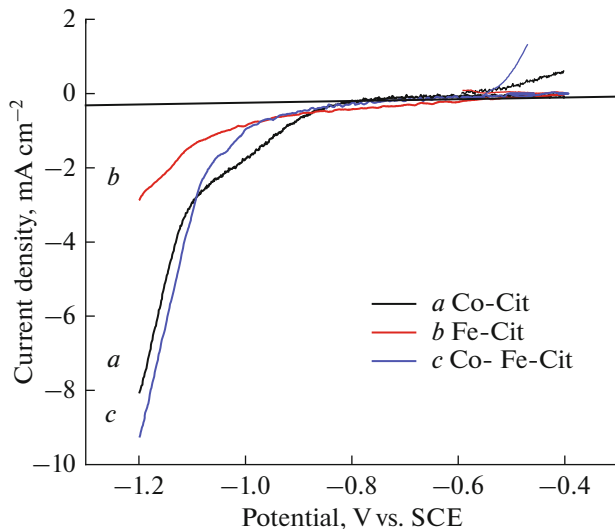


**Fig. 3.** Cathodic polarisation curves from CV plots at a scan rate  $10 \text{ mV s}^{-1}$  of electrodeposition for Co, Fe, and Fe–Co alloys. Bath condition: 0.05 M sodium citrate, 0.05 M  $\text{MgSO}_4$ , 0.40 M  $\text{H}_3\text{BO}_3$ , pH 4, and temperature  $25^\circ\text{C}$  with: (a) 0.1 M  $[\text{Co}^{2+}]$ , (b) 0.1 M  $[\text{Fe}^{2+}]$ , (c) 0.1 M  $[\text{Co}^{2+}]$ , and 0.1 M  $[\text{Fe}^{2+}]$ .

of iron deposition at 0.1M  $[\text{Fe}^{2+}]$  in Fig. 3, curve *b*, shows the onset of the cathodic reduction potential of  $\text{Fe}^{2+}$  at  $-0.94 \text{ V}$ . The cathodic polarisation in Fig. 3, curve (c), reveals the co-deposition of Co and Fe metals through the reduction of  $[\text{CoCitrate}]^-$  to  $\text{Co}^0$  and of  $[\text{FeCitrate}]^-$  to  $\text{Fe}^0$ . The observation of a unique cathodic potential of  $-0.88 \text{ V}$  for the reduction of both ions appears as the character of the electrodeposition of these alloys on the SS surface followed by a diffusion-controlled reduction of  $\text{H}^+$  ions. When the applied potential is more negative:  $-0.88 \text{ V}$ , there is a significant rise in the cathodic current density for the Fe–Co reduction till the current reaches a fixed value ( $-0.009 \text{ A}$ ) due to a stationary regime of  $[\text{Co}^{2+}]$  and  $[\text{Fe}^{2+}]$  around the SS cathode. This variance of the reduction potentials for deposition of Fe–Co alloys and Co or Fe is due to the simultaneous co-deposition of both Co and Fe at this potential range on the SS cathode.

Figure 4 demonstrates the effect of pH on the cathodic polarisations of the Fe–Co alloys deposition in a solution of 0.1 M  $[\text{Fe}^{2+}]$  and  $[\text{Co}^{2+}]$ , 0.05 M [sodium citrate], 0.05 M  $[\text{MgSO}_4]$ , and 0.04 M  $[\text{H}_3\text{BO}_3]$ . The initial reduction of Fe–Co alloys starts at  $-0.76 \text{ V}$ , at pH 2, with the evolution of hydrogen, and gradually shifts to  $-0.88 \text{ V}$ , when pH is 4. It was also demonstrated in Fig. 4 that with an increase in pH, the cathodic polarisation pattern and the reduction potentials are changed significantly, with changes in the reduction peak height. There is an anodic shift

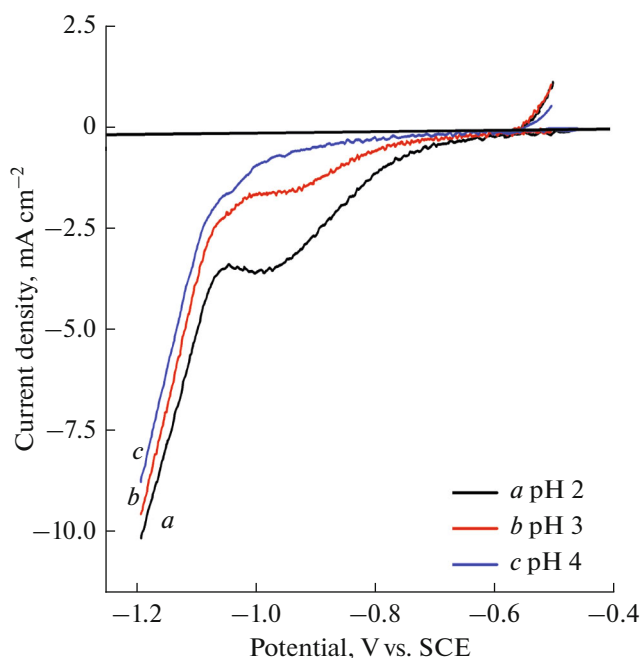


**Fig. 4.** Cathodic polarisation curves at different pH for electrodeposition of Fe–Co alloys at a scan rate of  $10 \text{ mV s}^{-1}$ . Bath condition:  $0.1 \text{ M } [\text{Fe}^{2+}]$ ,  $0.1 \text{ M } [\text{Co}^{2+}]$ ,  $0.05 \text{ M}$  sodium citrate,  $0.05 \text{ M } \text{MgSO}_4$ ,  $0.40 \text{ M } \text{H}_3\text{BO}_3$ , temperature  $25^\circ\text{C}$ , and: (a) pH 2, (b) pH 3, and (c) pH 4.

from the initial reduction potential value, with a flat nature of polarisation behaviour, via shifting pH from 2 to 4.

The influence of the ratio of concentration of the metal ions ( $[\text{Fe}^{2+}]/[\text{Co}^{2+}]$ ) on the electrodeposition of

Fe–Co alloys at pH 4 is presented in Fig. 5. Figure 5a demonstrates a decrease in  $[\text{Fe}^{2+}]$  with the fixed  $[\text{Co}^{2+}]$  whereas Fig. 5b depicts a decrease in  $[\text{Co}^{2+}]$ , with the fixed  $[\text{Fe}^{2+}]$ . There is no such appreciable variation in the reduction potential by decreasing  $[\text{Fe}^{2+}]$  as is also observed in Fig. 5a whereas the peak height of the reduction potential is decreased by decreasing  $[\text{Co}^{2+}]$  as observed in Fig. 5b. It may be envisaged from this study that  $[\text{Co}^{2+}]$  has more influence on the electrodeposition of the alloys when its value goes up from  $0.025$  to  $0.200 \text{ M}$  at a fixed  $[\text{Fe}^{2+}]$ .

The kinetic data such as the nucleation potential ( $E_n$ ), the crossover potential ( $E_{cp}$ ), and the nucleation overpotential ( $E_{nop}$ ) at different parametric conditions obtained from the cathodic polarisation plots are presented in Table 2. Each value of these parameters for the Fe–Co alloys lies in between the respective parameters of individual Fe and Co. The values are relatively closer to the value of Fe in the present investigation.

#### Cathode Potential

Figure 6 shows the influence of pH on the variation of the cathode potential (vs. SCE) with time at a constant current density of  $30 \text{ mA cm}^{-2}$  and temperature of  $25^\circ\text{C}$ . It can be seen that by increasing pH from 2 to 4, the cathode potential shifted to a less negative value with progress in time ( $-1.8$  to  $-1.72 \text{ V}$  during 60 min). The onset cathode potential was  $-2.21 \text{ V}$ , and then it decreased to  $-1.79 \text{ V}$  after one hour of electrodeposition at pH 2. The surfaces of the electrodeposits were very smooth and had a single solid solution of Fe-rich Fe–Co alloys (Co = 48.61 at %, Fe = 51.39 at %).

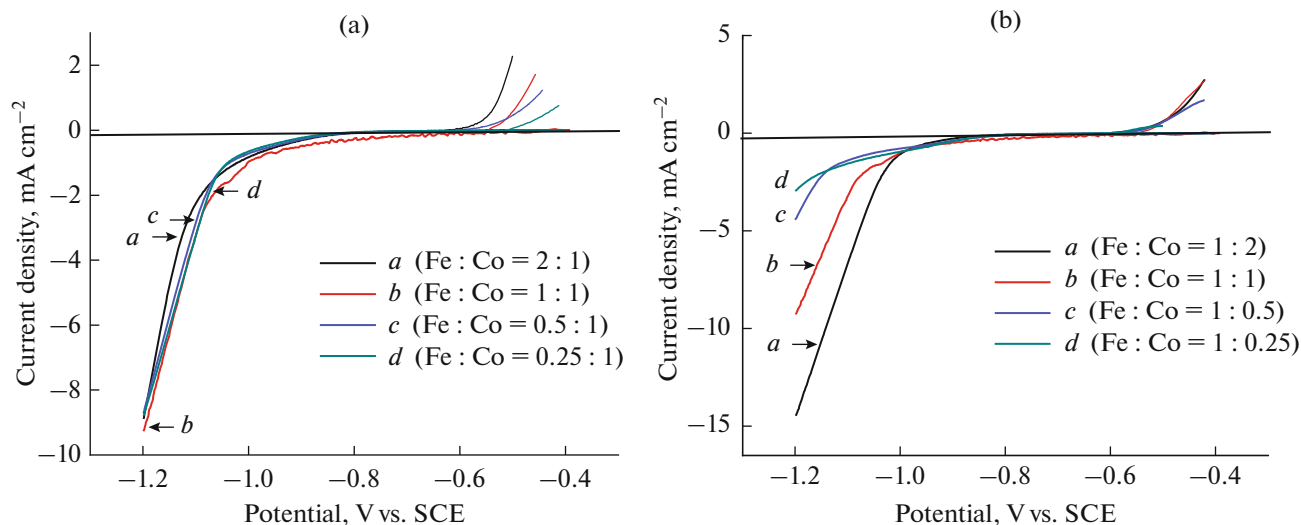


**Fig. 5.** Cathodic polarisation curves at different  $[\text{Fe}^{2+}]/[\text{Co}^{2+}]$  ratios for electrodeposition of Fe–Co alloys at a scan rate of  $10 \text{ mV s}^{-1}$ . Bath condition:  $0.05 \text{ M}$  sodium citrate,  $0.05 \text{ M } \text{MgSO}_4$ ,  $0.40 \text{ M } \text{H}_3\text{BO}_3$ , pH 4, temperature  $25^\circ\text{C}$  and: (a)  $0.025$ – $0.2 \text{ M } [\text{Fe}^{2+}]$  and  $0.1 \text{ M } [\text{Co}^{2+}]$ , and (b)  $0.025$ – $0.2 \text{ M } [\text{Co}^{2+}]$  and  $0.1 \text{ M } [\text{Fe}^{2+}]$ .

**Table 2.** Electrokinetic parameters,  $E_n$ ,  $E_{cp}$  and  $E_{nop}$  from cathodic polarisation plots at pH 4

$[\text{Fe}^{2+}]$ , M	$[\text{Co}^{2+}]$ , M	$E_n$ , V	$E_{cp}$ , V	$E_{nop}$ , V	$i_o$ , $\text{mA cm}^{-2}$	$\beta_c$ , $\text{mV decd}^{-1}$	$\alpha$
0.1	—	-0.943	-0.674	0.269	$2.46 \times 10^{-3}$	227.8	0.11
—	0.1	-0.835	-0.584	0.251	$1.07 \times 10^{-3}$	131.3	0.19
0.1	0.1	-0.884	-0.563	0.321	$2.28 \times 10^{-3}$	124.9	0.20
0.2	0.1	-0.916	-0.571	0.345	$5.25 \times 10^{-3}$	305.2	0.08
0.05	0.1	-0.893	-0.574	0.319	$2.28 \times 10^{-3}$	282.6	0.09
0.025	0.1	-0.842	-0.501	0.341	$1.27 \times 10^{-3}$	112.9	0.22
0.1	0.2	-0.844	-0.566	0.278	$7.01 \times 10^{-4}$	147.4	0.18
0.1	0.05	-1.013	-0.551	0.462	$2.36 \times 10^{-4}$	135.2	0.19
0.1	0.025	-1.168	-0.592	0.576	$4.02 \times 10^{-4}$	105.4	0.24

$E_n$ , nucleation potential;  $E_{cp}$ , crossover potential;  $E_{nop}$ , nucleation over potential;  $i_o$ , exchange current density;  $\beta_c$ , cathodic Tafel constant, and  $\alpha$ , transfer coefficient.

There is a similar order of decreasing tendency of the cathode potential observed at pH 3 and 4. The cathode potential at pH 3 starts from  $-2.10$  V and ends at  $-1.75$  V. The lowest value of the cathodic potential is detected at pH 4 where it starts from  $-1.96$  V and ends at  $-1.72$  V. The electro-deposits are usually smooth, uniform, and composed of cobalt-rich Fe–Co alloys (Co = 54.27 at %, Fe = 45.73 at %).

The trend of the cathode potentials (vs. SCE) with the current density at pH 4 and the temperature  $25^\circ\text{C}$  is also analysed. It was observed that with an increase in the current density, the cathode potentials shift to the cathodic direction, and the shift is towards the

anodic direction in case the current density progresses with time. The variation of the cathode potential with time is not that appreciable within  $30$  to  $50$   $\text{mA cm}^{-2}$  of the applied current density, whereas the shifting trend to the anodic direction is very much significant in case of the applied current density of  $60$  and  $70$   $\text{mA cm}^{-2}$ . The initial cathode potential of  $-1.95$  V at the applied current density of  $30$   $\text{mA cm}^{-2}$  was found to shift to a more cathodic potential of  $-4.40$  V at an applied current density of  $70$   $\text{mA cm}^{-2}$ . Due to higher cathode potentials, at the highest applied current density of  $70$   $\text{mA cm}^{-2}$ , the deposit quality changes from smooth and uniform, as was at a lower applied current density, to non-uniform, rough, and powdery.

In addition, the effect of respective  $[\text{Fe}^{2+}]/[\text{Co}^{2+}]$  due to  $[\text{Co}^{2+}]$  and  $[\text{Fe}^{2+}]$  ( $0.2$ – $0.025$  M) on the cathode potential at the fixed current density of  $30$   $\text{mA cm}^{-2}$  was also investigated. It was observed that with an increase in  $[\text{Co}^{2+}]$ , the initial cathode potential shifts to a more negative value ( $-1.72$  V to  $-2.11$  V) whereas there is a uniform positive shift in the cathode potential with time for each  $[\text{Co}^{2+}]$  even if it decreases from  $0.2$  to  $0.025$  M. A similar trend was noticed in the variations of  $[\text{Fe}^{2+}]$ . The initial value of the cathode potential shifted from  $-1.69$  to  $-2.10$  V, and then there was a gradual positive shift with time as  $[\text{Fe}^{2+}]$  increase from  $0.025$  to  $0.2$  M.

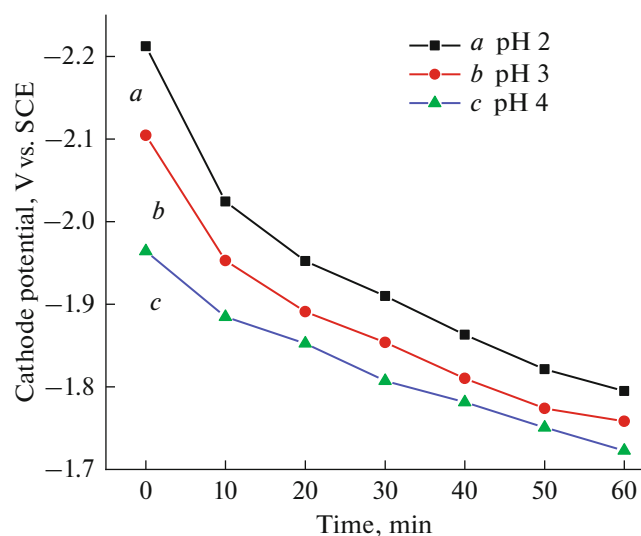


**Fig. 6.** Cathode potential vs. time at different pH. Bath condition:  $0.1$  M  $[\text{Fe}^{2+}]$ ,  $0.1$  M  $[\text{Co}^{2+}]$ ,  $0.05$  M sodium citrate,  $0.05$  M  $\text{MgSO}_4$ ,  $0.40$  M  $\text{H}_3\text{BO}_3$ , temperature  $25^\circ\text{C}$ , current density  $30$   $\text{mA cm}^{-2}$  and: (a) pH 2, (b) pH 3, and (c) pH 4.

### Current Efficiency

The effects of variations of the concentrations of the metal precursors, of the current density, and of temperature on the current efficiency of the electrodeposition are reflected in Figs. 7 and 8. Figure 7 shows the effect of varied  $[\text{Fe}^{2+}]/[\text{Co}^{2+}]$  in a range of  $[\text{Co}^{2+}]$  and  $[\text{Fe}^{2+}]$  ( $0.200$ – $0.025$  M) on the current efficiency at pH 4. It is observed in Fig. 7, curve a, that with an

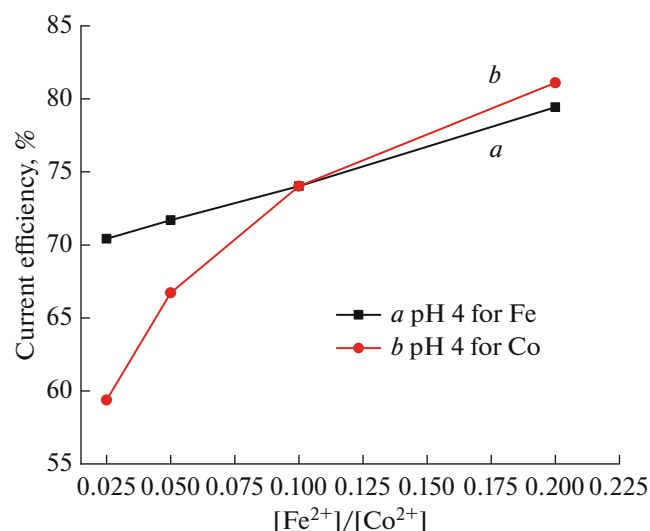


**Fig. 7.** Current efficiency vs.  $[\text{Fe}^{2+}]/[\text{Co}^{2+}]$  at pH 4. Bath condition: 0.05 M sodium citrate, 0.05 M  $\text{MgSO}_4$ , 0.40 M  $\text{H}_3\text{BO}_3$ , temperature 25°C, and current density 30  $\text{mA cm}^{-2}$ : (a) 0.025–0.2 M  $[\text{Fe}^{2+}]$  and 0.1 M  $[\text{Co}^{2+}]$ , (b) 0.025–0.2 M  $[\text{Co}^{2+}]$ , and 0.1 M  $[\text{Fe}^{2+}]$ .

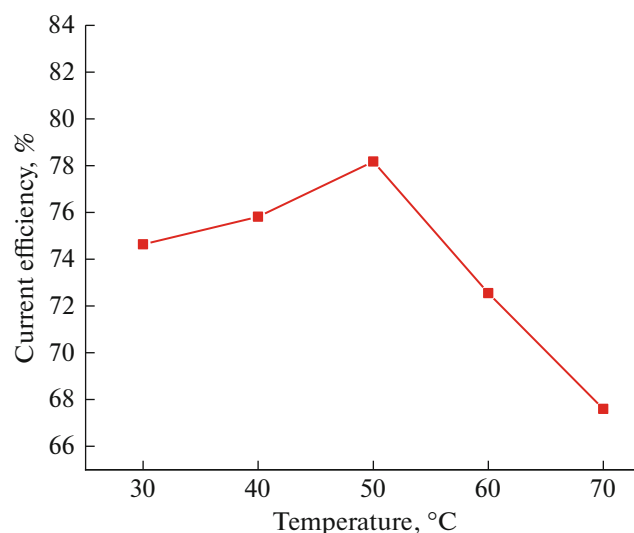


**Fig. 8.** Current efficiency vs. temperature for Fe–Co electrodeposition. Bath condition: 0.1 M  $[\text{Fe}^{2+}]$ , 0.1 M  $[\text{Co}^{2+}]$ , 0.05 M sodium citrate, 0.05 M  $\text{MgSO}_4$ , 0.40 M  $\text{H}_3\text{BO}_3$ , and current density 30  $\text{mA cm}^{-2}$ .

increase in  $[\text{Fe}^{2+}]$  containing fixed  $[\text{Co}^{2+}]$  of 0.1 M, the current efficiency increases from 70.42 to 79.43%. Similarly, Fig. 7, curve *b*, demonstrates that the current efficiency increases from 59.38 to 81.10% by increasing  $[\text{Co}^{2+}]$  from 0.025 to 0.20 M, with fixed  $[\text{Fe}^{2+}]$  of 0.10 M. But with an increase in the applied current density from 30 to 70  $\text{mA cm}^{-2}$ , the current efficiency decreases from 74.02 to 56.5%.

Figure 8 presents the effect of temperature on the current efficiency at the applied current density of 30  $\text{mA cm}^{-2}$  and at pH 4. The current efficiency increases from 74.63 to 78.17% with an increase in temperature up to 50°C and then falls to 67.6% when temperature reaches 70°C. This may be due to more hydrogen evolution reactions [31] after 50°C for which a decrease in the CCE is observed.

#### *Fe–Co Deposit Structure*

Figures 9a, 9b show the XRD data of the electroplated Fe–Co alloys at pH 2, 3, and 4, of two different concentrations of  $[\text{Co}^{2+}]$  and  $[\text{Fe}^{2+}]$  at pH 4. The diffraction peaks corresponding to Fe–Co alloys are observed on all curves showing the nano-crystalline structure of the deposits. The peaks located at 44.72° and 82.41° correspond to Fe–Co (110) and Fe–Co (211) of the cubic structure. There are no other different peaks observed in Fig. 9 except those of Fe–Co (110), Fe–Co (200), and Fe–Co (211) of the cubic structure. As the data in the insets in Fig. 9 reveal, the diffraction peaks of Fe–Co (110) show a stronger preferred orientation than that of the remaining Fe–Co

(200) and Fe–Co (211) at any pH condition. Besides, the inset in Fig. 9a shows that there is a slight shift of the peaks towards a lower angle with increasing pH. It indicates an increase in the lattice constant at higher pH. This is because of a relatively larger atomic radius of Fe of 0.110 nm than that of Co of 0.104 nm as agreed by others [32, 33].

The average crystallite size ( $D$ ) is calculated using the Scherrer formula  $D = K\lambda/\beta\cos\theta$  [17, 27]. The average crystallite size of the deposited alloys increases from 18 nm through 30 to 36 nm, at pH 2, 3, and 4, respectively. Similarly, the average crystallite size of the deposited alloys shown in Fig. 9b also increased from 28 nm (plot *d*) to 32 nm (plot *e*) with an increase in  $[\text{Co}^{2+}]$  from 0.1 to 0.2 M.

At pH 2 and 3, only two reflection peaks at  $2\theta$  of 44.72° and 82.41° are seen that correspond to the Bragg reflection planes (110) and (211). But at pH 4, three reflection peaks at  $2\theta$  of 44.72°, 65.09°, and 82.41° are seen that correspond to the reflection planes (110), (200), and (211). The reflection patterns are found to be same in Fig. 9b with different  $[\text{Co}^{2+}]$  and  $[\text{Fe}^{2+}]$ . In all conditions, the (110) peak is found to be the strongest peak. The reflection patterns reveal the single-phase pure Fe–Co alloys with a bcc structure [18]. There are no additional reflection peaks observed due to the individual pure Fe and Co, which confirms the formation of the single solid solution of Fe–Co.

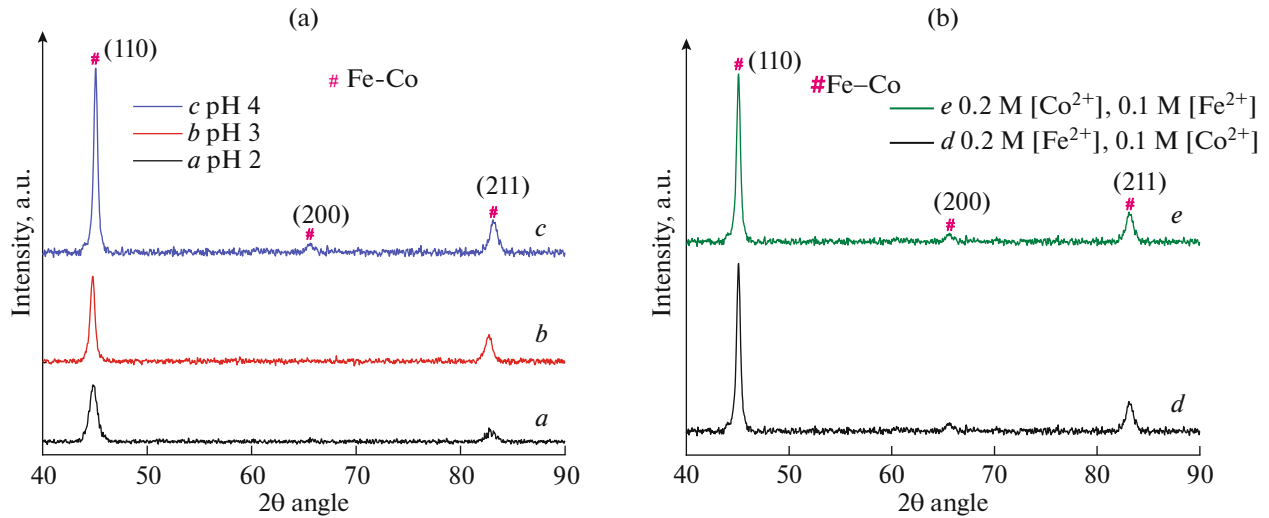


**Fig. 9.** XRD analysis of Fe–Co alloys. Bath condition: 0.05 M sodium citrate, 0.05 M MgSO<sub>4</sub>, 0.40 M H<sub>3</sub>BO<sub>3</sub>, temperature 25°C, current density 30 mA cm<sup>-2</sup>: (a) 0.1 M [Fe<sup>2+</sup>], 0.1 M [Co<sup>2+</sup>] (a) pH 2, (b) pH 3, and (c) pH 4, and (b) pH 4 (d) 0.2 M [Fe<sup>2+</sup>], 0.1 M [Co<sup>2+</sup>], (e) 0.1 M [Fe<sup>2+</sup>], and 0.2 M [Co<sup>2+</sup>].

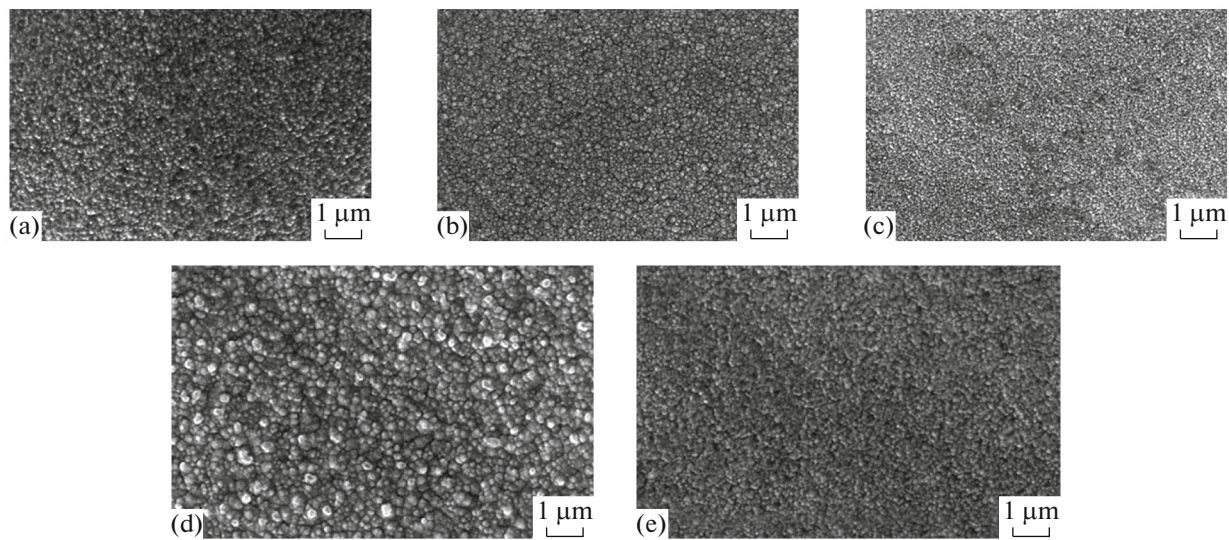


**Fig. 10.** SEM micrographs of Fe–Co alloys electrodeposited in different solution compositions. Bath condition: 0.05 M sodium citrate, 0.05 M MgSO<sub>4</sub>, 0.40 M H<sub>3</sub>BO<sub>3</sub>, temperature 25°C, current density 30 mA cm<sup>-2</sup>, and (a) 0.1 M [Fe<sup>2+</sup>], 0.1 M [Co<sup>2+</sup>] pH 4, (b) 0.1 M [Fe<sup>2+</sup>], 0.1 M [Co<sup>2+</sup>] pH 3, (c) 0.1 M [Fe<sup>2+</sup>], 0.1 M [Co<sup>2+</sup>], pH 2, (d) 0.2 M [Fe<sup>2+</sup>], 0.1 M [Co<sup>2+</sup>], pH 4, and (e) 0.1 M [Fe<sup>2+</sup>], 0.2 M [Co<sup>2+</sup>], pH 4.

#### *Fe–Co Deposit Surface Morphology and Composition Analysis*

Figure 10 shows the surface morphology of the electroplated samples at different pH and concentration conditions studied via SEM. The EDS results on the composition of the electroplated Fe–Co alloys are presented in Table 3. The surface morphology and the metal composition in the alloys are considered to be strongly influenced by the pH of the electrolytic solution [25, 32, 33]. The elemental analysis has revealed

the presence of only Fe and Co without any impurity. The Fe–Co alloy has more iron content (51.39 at %) at pH 2, but it decreases gradually to 45.73 at % with an increase in pH. The cobalt content increases from 48.61 to 54.27 at %, with an increase of pH from 2 to 4. In all these cases, the structure of the deposits is found to be spherical, and the average size of particles is in the nanometer range: 61.50, 96.62, and 120 nm, at pH 2, 3, and 4, respectively, as estimated by using the software Image J. The particle size in the deposits



**Table 3.** Composition of electrodeposited Fe–Co alloys at different pH and concentrations

Metal precursors	pH	Element	wt %	at %
0.1 M [Fe <sup>2+</sup> ],	4	Fe	44.39	45.73
0.1 M [Co <sup>2+</sup> ]		Co	55.61	54.27
0.1 M [Fe <sup>2+</sup> ],	3	Fe	47.12	48.47
0.1 M [Co <sup>2+</sup> ]		Co	52.88	51.33
0.1 M [Fe <sup>2+</sup> ],	2	Fe	50.06	51.39
0.1 M [Co <sup>2+</sup> ]		Co	49.94	48.61
0.2 M [Fe <sup>2+</sup> ],	4	Fe	65.24	64.33
0.1 M [Co <sup>2+</sup> ]		Co	34.76	35.67
0.1 M [Fe <sup>2+</sup> ],	4	Fe	30.16	31.42
0.2 M [Co <sup>2+</sup> ]		Co	69.84	68.61

obtained via SEM at different pH indicates a relatively smooth surface, with small and uniform grains at lower pH as compared to those at higher pH. The deposits at higher pH are larger grains of nearly 120 nm in size than 61.50 nm size obtained at the lowest pH. Figures 10d and 10e present the SEM analysis data of the Fe–Co alloys deposited at two different concentrations of [Co<sup>2+</sup>] and [Fe<sup>2+</sup>] at pH 4. It was observed that by increasing [Fe<sup>2+</sup>] two-fold, in comparison with [Co<sup>2+</sup>], the percentage of iron increases to 64.33 at % in the deposit. Similarly, the percentage of cobalt in the deposit increases to 68.61 at % by maintaining the [Co<sup>2+</sup>] value twice higher than that of [Fe<sup>2+</sup>]. The average size of particles of the deposits was found to be 164.32 and 105.47 nm, respectively.

#### Magnetic Properties

The Fe–Co alloys with relative iron contents ranging from around 31 to 64 at % were successfully deposited, with a uniform surface structure on the SS substrate, as presented in Fig. 10. The iron contents in the deposits were found to increase at higher [Fe<sup>2+</sup>] in the electrolytic bath, as reported elsewhere [19, 34, 35], which significantly influences the magnetic properties of the deposits. It was also reported that  $B_s$  and  $H_c$  were also grossly affected [35, 36] by the iron content in the deposit. In particular, the composition of the deposit and the growth of the films affect the deposit texture and crystallographic orientation, which, in turn, has an impact on the  $B_s$ . The intensity index of the bcc (110) plane of the electroplated Fe–Co films is also considered to have a significant contribution into the  $B_s$  [36]. Similarly, the changes induced in  $H_c$  may be due to the grain size and the roughness of deposit surface [35]. It was also stated elsewhere that nano-sized grains show a low  $H_c$  value owing to a low and random magnetic anisotropy whereas small-sized grains pro-

duce a high  $H_c$  because of a large volume of grain boundaries. Therefore, the magnetic property of the deposits may be attributed partly to their physical structure that affects the crystalline anisotropy and directions of magnetization alignment [34–36]. In the present study, in addition to the iron content growth (31 to 64 at %), the crystallographic orientation of the Fe–Co deposits of (110), (211), and (200), and the average grain sizes of 61.50, 96.62, and 120 nm are all within the reported range. Further studies in similar lines are needed to correlate the data and to bring out the effect for filling up the gap as hardly any conclusive studies are available on this aspect.

#### CONCLUSIONS

The specific research outcomes of the present study are presented as follows:

- (1) The Fe–Co alloy thin films having nano-crystalline spherical deposits were successfully electrodeposited on SS with a higher current efficiency (>80%) from a sulfate bath containing sodium citrate as a complexing agent.
- (2) The transfer coefficient ( $\alpha$ ) values confirm the unsymmetrical cathodic and anodic processes of electrodeposition.
- (3) The XRD diffraction peaks of the electrodeposits confirm Fe–Co alloys and indicate a micro-crystalline structure with Fe–Co (110) as the preferred orientation at all pH values.
- (4) The percentage of cobalt and iron content increases with an increase in the concentration of one of the metal ions keeping the other one constant at pH 4. The cobalt content increases from 48.61 to 54.27 at % with an increase in pH 2 to 4.
- (5) The average grain size and the crystallographic orientation of the deposited alloys confirm that the studied alloy may serve as a suitable candidate to exhibit better magnetic property.
- (6) The intensity index of the bcc (110) plane of the electroplated Fe–Co alloys is considered to play a critical role for  $B_s$ . The changes induced in  $H_c$  may be due to the average grain size and to the roughness of the deposit surface.

#### ACKNOWLEDGMENTS

The authors acknowledged the support of the Kalinga Institute of Industrial Technology Deemed to be University, Bhubaneswar, India, and the Institute of Minerals and Materials Technology, Bhubaneswar, India, for the characterisation facilities of the alloys.

#### CONFLICT OF INTEREST

The authors declare that they have no conflicts of interest.

## AUTHOR CONTRIBUTIONS

The experiments were conducted by Santosh Kumar Nathsharma and Sasmita Mishra and were supervised by Krushna Gopal Mishra and Raja Kishore Paramguru. All authors have gone through and then recommended the manuscript for the outward transmission to the Journal.

## REFERENCES

- Khan, K., Rehman, S., Rehman, H.U., and Khan, Q., Synthesis and application of magnetic nanoparticles, in *Nanomagnetism*, Altrincham: One Central Press, 2014, ch. 6.
- Chansena, A. and Sutthiruangwong, S., Corrosion behavior of electrodeposited Co–Fe alloys in aerated solutions, *J. Magn. Magn. Mater.*, 2017, vol. 429, no. 5, p. 251.
- Zhang, J., Muller, J.O., Zheng, W., Wang, D., et al., Individual Fe–Co alloy nanoparticles on carbon nanotubes: Structural and catalytic properties, *Nano Lett.*, 2008, vol. 8, no. 9, p. 2738.
- Kidosaki, T., Takase, S., and Shimizu, Y., Electrodeposited cobalt–iron alloy thin-film for potentiometric hydrogen phosphate-ion sensor, *J. Sens. Technol.*, 2012, vol. 2, no. 3, p. 95.
- Shao, I., Romankiw, L.T., and Bonhote, C., Stress in electrodeposited Co–Fe alloy films, *J. Cryst. Growth*, 2010, vol. 312, no. 8, p. 1262.
- Shao, I., Chen, M.W., Cammarata, R.C., Searson, P.C., et al., Deposition and characterization of Fe<sub>0.55</sub>Co<sub>0.45</sub> nanowires, *J. Electrochem. Soc.*, 2007, vol. 154, no. 11, p. D572.
- Liu, X., Evans, P., and Zangari, G., Electrodeposited Co–Fe and Co–Fe–Ni alloy films for magnetic recording write heads, *IEEE Trans. Magn.*, 2000, vol. 36, no. 5, p. 3479.
- Kim, S.S., Kim, S.T., Ahn, J.M., and Kin, K.H., Magnetic and microwave absorbing properties of Co–Fe thin films plated on hollow ceramic microspheres of low density, *J. Magn. Magn. Mater.*, 2004, vol. 271, no. 1, p. 39.
- Li, Z.-M., Xu, F.-Q., Wang, L.-W., Wang, J., et al., X-ray magnetic circular dichroism measurement of Fe–Co alloy films prepared by electrodeposition, *Chin. Phys. Lett.*, 2007, vol. 24, no. 9, p. 2667.
- Koza, J.A., Uhlemann, M., Gebert, A., and Schultz, L., The effect of magnetic fields on the electrodeposition of Co–Fe alloys, *Electrochim. Acta*, 2008, vol. 53, no. 16, p. 5344.
- Sourmail, T., Near equiatomic FeCo alloys: Constitution, mechanical and magnetic properties, *Prog. Mater. Sci.*, 2005, vol. 50, no. 7, p. 816.
- Sundar, R.S. and Deevi, S.C., Soft magnetic Fe–Co alloys: alloy development, processing, and properties, *Int. Mater. Rev.*, 2005, vol. 50, no. 3, p. 157.
- Hou, X.W., Liu, S.B., Yang, S.L., Li, J.P., et al., Electrical and magnetic properties of electrodeposited Fe-based alloys used for thin film transformer, *Sci. Chin. Sci.*, 2013, vol. 56, no. 1, p. 84.
- Laughlin, D.E. and McHenry, M.E., Nanoscale materials development for future magnetic applications, *Acta Mater.*, 2000, vol. 48, no. 1, p. 223.
- Toth, B.G., Peter, L., Pogany, L., Revesz, A., and Bakonyi, I., Preparation, structure and giant magnetoresistance of electrodeposited Fe–Co/Cu multilayers, *J. Electrochem. Soc.*, 2014, vol. 161, no. 4, p. D154.
- Yanai, T., Shiraishi, K., Watanabe, Y., Ohgai, T., et al., Magnetic Fe–Co films electroplated in deep-eutectic-solvent-based plating bath, *J. Appl. Phys.*, 2015, vol. 117, p. 17A925-1.
- Sides, W., Kassouf, N., and Huang, Q., Electrodeposition of ferromagnetic FeCo and FeCoMn alloy from choline chloride based deep eutectic solvent, *J. Electrochem. Soc.*, 2019, vol. 166, no. 4, p. D77.
- Soundararaj, A. and Mohanty, J., Impact of deposition potential on structural and magnetic properties of nanocrystalline Co–Fe alloy thin film, *Surf. Eng. Appl. Electrochem.*, 2020, vol. 56, no. 2, p. 159.
- Qin, X.Y., Kim, J.G., and Lee, J.S., Synthesis and magnetic properties of nanostructured  $\gamma$ -Ni–Fe alloys, *Nanostruct. Mater.*, 1999, vol. 11, no. 2, p. 259.
- Liu, X., Evans, P., and Zangari, G., Electrodeposited Co–Fe and Co–Fe–Ni alloy films for magnetic recording write heads, *IEEE Trans. Magn.*, 2000, vol. 36, no. 5, p. 3479.
- Tartaj, P., del Puerto Morales, M., Veintemillas-Verdaguer, S., González-Carreño, T., et al., The preparation of magnetic nanoparticles for applications in biomedicine, *J. Phys. D: Appl. Phys.*, 2003, vol. 36, p. R182.
- Balachandran, P., Yow, H.K., Ong, B.H., Tan, K.B., et al., Surface morphology and electrical properties of pulse electrodeposition of Ni–Fe films on copper substrates in ultrasonic field, *Int. J. Electrochem. Sci.*, 2011, vol. 6, no. 8, p. 3564.
- Saravanan, G. and Mohan, S., Electrodeposition of Fe–Ni–Cr alloy from deep eutectic system containing choline chloride and ethylene glycol, *Int. J. Electrochem. Sci.*, 2011, vol. 6, no. 5, p. 1468.
- Hassan, H.B. and Hamid, Z.A., Electrodeposited Cu–CuO composite films for electrochemical detection of glucose, *Int. J. Electrochem. Sci.*, 2011, vol. 6, no. 11, p. 5741.
- Qiang, C., Xu, J., Xiao, S., Jiao, Y., et al., The influence of pH and bath composition on the properties of Fe–Co alloy film electrodeposition, *Appl. Surf. Sci.*, 2010, vol. 257, no. 5, p. 1371.
- Lu, W., Huang, P., He, C., and Yan, B., Compositional and structural analysis of FeCo films electrodeposited at different temperatures, *Int. J. Electrochem. Sci.*, 2012, vol. 7, no. 12, p. 12262.
- Nathsharma, S.K., Mishra, S., Mishra, K.G., and Paramguru, R.K., The effect of bath parameters on the electrocrystallisation of Co<sub>x</sub>–Cu<sub>100-x</sub> alloys on stainless steel cathode, *Trans. Indian Inst. Met.*, 2020, vol. 73, no. 2, p. 377.
- Srimathi, S.N., Mayanna, S.M., and Sheshadri, B.S., Electrodeposition of binary magnetic alloys, *Surf. Technol.*, 1982, vol. 16, p. 277.
- Bertazzoli, R. and Pletcher, D., Studies of the mechanism for the electrodeposition of Fe–Co alloys, *Electrochim. Acta*, 1993, vol. 38, no. 5, p. 671.

30. El Rehim, S.S.A., Khaled, K., Abulkibash, A.M.S., and Emad, M., Electroplating of Co–Fe alloys from aqueous acetate baths, *Trans. Inst. Met. Finish.*, 2000, vol. 78, no. 1, p. 41.
31. Jiao, P., Duan, N., Zhang, C., Xu, F., Chen, G., Li, J., et al., The effect of cobalt ion on the hydrogen evolution reaction in sulfate solution, *Int. J. Hydrogen Energy*, 2016, vol. 41, no. 40, p. 17793.
32. Joshi, H.H. and Kulkarni, R.G., Susceptibility, magnetization and Mossbauer studies of the Mg–Zn ferrite system, *J. Mater Sci.*, 1986, vol. 21, no. 6, p. 2138.
33. Kakatkar, S.V., Kakatkar, S.S., Patil, R.S., Sankpal, A.M., et al., X-ray and bulk magnetic properties of the Ni–Zn ferrite system, *Phys. Status Solidi B*, 1996, vol. 198, no. 2, p. 853.
34. Najafi, A. and Nematipour, K., Synthesis and magnetic properties evaluation of monosized Fe–Co alloy nanoparticles through microemulsion method, *J. Supercond. Nov. Magn.*, 2017, vol. 30, no. 9, p. 2647.
35. Osaka, T., Asahi, T., Kawaji, J., and Yokoshima, T., Development of high-performance magnetic thin film for high-density magnetic recording, *Electrochim. Acta*, 2005, vol. 50, no. 23, p. 4576.
36. Osaka, T., Electrodeposition of highly functional thin films for magnetic recording devices of the next century, *Electrochim. Acta*, 2000, vol. 45, no. 20, p. 3311.